Journal of
Marine Science and Engineering

Article

Scale Effects on a Tip Rake Propeller Working in Open Water

Adrian Lungu

Department of Naval Architecture, "Dunarea de Jos" University of Galati, 800008 Galati, Romania; adrian.lungu@ugal.ro

Received: 7 September 2019; Accepted: 6 November 2019; Published: 8 November 2019

Abstract: The scale effect on the accuracy of a numerical simulation in ship hydrodynamics represents an important issue of the propeller numerical analysis. To grasp a better understanding on the influence of this effect, an introspection on the performances of an unconventional propeller is proposed in the present study. The paper describes an investigation of the performances of a tip rake propeller recently chosen as benchmark by the International Towing Tank Conference organization (ITTC hereafter). The numerical simulation is carried out by making use of the ISIS-CFD solver, part of the Fine™/Marine package available in the NUMECA suite. The solver is based on the finite volume method to build the spatial discretization of the governing equations. The incompressible unsteady Reynolds Averaged Navier-Stokes Equations (RANSE) are solved in a global approach. Reported solutions are compared with the experimental data provided by Schiffbau-Versuchsanstalt (SVA) Potsdam GmbH to validate the accuracy of the numerical approach. Since for the full scale the experimental data could not be possible, the ITTC'78 extrapolation method-based proposed by the SVA Potsdam has been taken as a basis for comparisons and discussions. A set of remarks will conclude the paper by providing some guidelines for further approaches in terms of the particulars of the numerics that may be further employed in similar studies.

Keywords: TRP propeller; viscous flow simulation; DES turbulence model; ITTC benchmark; scale effect

1. Introduction

Although the problem of simulating the flow around a propeller working in open water (POW hereafter) conditions does not represent a troublesome subject from the numerical point of view, the extrapolation of the solution computed for a model to the corresponding full scale remains one of the most challenging tasks since the reported achievements in the field are still scarce and contradictory. This is because certain issues such as the intrinsic aspects of the boundary layer dimension and structure, which is crucially important in any viscous flow simulation, the influence of the solid surface quality may influence the reliability of the solution at the full scale, the transposition of the solution from the model to the full scale are still to be clarified. Under such circumstances, the Propulsion Committees of the 27th and 28th ITTC launched a computational campaign in which a conventional highly skewed propeller, and an unconventional propeller with the tip-rake were subjected for numerical studies devoted to clarify how the propeller scale effects may be accurately predicted as well as to address the eventual drawbacks of the methodology.

The extrapolation of the solutions from the model scale to the full scale has always represented a subject of a wide debate among those involved in the propeller hydrodynamics [1,2]. Generally speaking, the numerical predictions performed at model scale are more challenging than those at full scale due to the possible simultaneous cohabitation of laminar and turbulent flow regimes and to the subsequent difficulty in the accurate prediction of the transition to the turbulence in the computations.

Since the flow separation may be present at model scale, but it may be absent at full scale, one may raise a question whether the extrapolation of the solution from the model to the full scale may be a reliable procedure or not. From this point of view, any additional clarification on the details of the best method to use for a proper transposition of the results is needed.

Existing differences in thrust and torque coefficients between a model and a full scale propeller is still representing a subject of interest exerted by the scientific community coordinated by ITTC propeller committee. This is mainly due to the fact that predicting the powering performance at full scale, requires to apply the ITTC'78 method for scaling the open-water performances [3]. Nevertheless, it became already accepted that traditional scaling methods fail to reflect correctly the effect of the Reynolds number on the hydrodynamic characteristics, in particular for high skew and tip loaded propellers. Alternatively, it may be possible to take advantage of the fact that at a sufficiently high *Re* number the POW experiments become independent of scaling. However, the second approach requires suitable model facilities and equipment of a large scale, which is still prohibitive from the point of view of the associated costs. Because of all those mentioned before, for unconventional propellers there were claims for a revision of the technique because the actual procedure may not be able to capture the scaling effects, since the original ITTC'78 procedure uses a similarity assumption that reduces the spanwise quantities to a single value of 0.75 *R* [4].

Since the performance of a full scale propeller is not commonly available, novel methodologies have been proposed to scale the open-water data from tests performed at different *Re* numbers to the full scale propeller [5,6]. The power and shaft revolutions were predicted on a series of different scaling methods. These predictions were compared to the existing experimental data to quantify the quality of each scaling method. The standard deviations of the normalized model–ship power correlation factors were calculated as a measure of the quality of the prediction. All the investigated methods showed a mean value of the correlation factor of about 1.

Improving propulsive efficiency remains a continuous aim for naval architects. Designing unconventional geometries such as the tip rake propellers (TRP in the following) may represent a good choice since the performances of a classic propeller geometry have already failed in showing promising expectations in obtaining a better efficiency. Propellers with special tip geometries may present new challenges to the ITTC method for predicting the associated scale effects since it was already found through numerical simulations that the scale effects on the Kappel and contracted loaded tip (CLT hereafter) propellers are larger than those on conventional propellers [7,8].

A large number of studies were devoted in the past two decades to imagine atypical geometries expected to contribute to better hydrodynamic performances such as those reported in [9–11]. Kappel geometries proposed in [9] as well as the CLT propellers proposed in [10] proved to be encouraging choices to improve the efficiency by shifting the spanwise circulation distribution towards the tip of the blade by using geometric innovations to prevent the losses over the tip, otherwise hard to avoid. To get a better insight into the hydrodynamic loadings including steering moment of open thrusters, numerical investigations and model tests were performed in [11]. Experiments were carried out under both positive and negative advance speeds and azimuth angles from −90° to +90°. Measurements of propeller thrust and torque, total thrust, side force and steering moment at different azimuth angles and at different advance coefficients were presented and discussed, as the associated numerical analysis solutions. The numerical treatment was based on the VOF technique, the $\gamma - Re_\theta$ model was chosen to simulate the transition to turbulence inside the viscous layer in which the no-slip boundary conditions were imposed on all solid surfaces.

Krasilnikov et al. have studied the influences exerted by the blade skew, loading and area ratio on scaling using the commercial ANSYS-FLUENT solver with the k-ω SST turbulence model in [12]. Simultaneously, Müller et al. used in [13] the ANSYS-CFX solver with the same turbulence model to numerically analyze a variety of propellers at both model and full scales in open water working condition. Another numerical investigation on scaling the open water performance for five- and four -bladed propellers based in using FLUENT and the k-ω SST model for both high and low *Re* numbers flow conditions was reported in [14]. Studying the flow through simulations performed at *Re* numbers ranging from model scale to full scale, the authors proved by means of comparisons of the computed solutions with the experimental data that a large part of the boundary layer on the blade surface is laminar at the model scale Reynolds number. Aside of that, it has been shown that the dependencies of the thrust and torque coefficients on the *Re* number may be regarded as being straightforward if the *Re* number is sufficiently large. Severe limitations on turbulence modeling were reported in [15] and the need for a good grid quality has been stressed from the point of view of how a solid wall should be better treated in a turbulence model. A detailed investigation of the scale effects on the open water characteristics of a moderately skewed four-bladed controllable pitch propeller, based on the Star-CCM+ software is presented in [16]. Computations were performed in both model and full scale conditions and the authors concluded that the scale effects on the open water thrust and torque characteristics were found to be in a comparable range with those obtained at the open water test experiments, thus emphasizing the performances of the solver. Another numerical study of the scale effects was carried out on the Potsdam Propeller Test Case II propeller P1727 (PPTC II hereafter) in [17]. The investigation was based on the RANS simulations by using the FLUENT solver, in which the low Reynolds number option in the SST k–ω model was adopted at model scale, together with fine prism grids to resolve properly the viscous sub-layer. On the contrary, at full scale a standard wall function was used. The scale-effect corrections yielded by the RANS simulations were compared to those obtained from the ITTC method and the conclusion was that up to some extent the RANS and ITTC-based predictions for full scale efficiency agreed satisfactorily.

The present paper describes a numerical investigation of the unsteady viscous flow around the PPTC II tip-rake propeller and the solutions are validated through comparisons with the experimental data provided by SVA Potsdam for the model, whereas the ITTC scaling method was applied to the open water test results to obtain the full scale CFD performances [18]. Computations are performed for a series of five different advance ratio coefficients in both model and full scale conditions. The software package used to solve the task of the present research is Fine™/Marine, whose main solver is ISIS-CFD, which is a finite volume based one. Comparisons with the experimental data show a good agreement, a fact that may suggest both the appropriateness of the numerical approach and the robustness of the flow solver.

2. Geometric Setup and Computational Mesh

2.1. Propeller Characteristics

The fixed-pitch P1727 TRP propeller shown in Figure 1 will be considered in the present study, for which the open water computation is performed. The geometry has been designed by SVA Potsdam [18] as the 2018 ITTC benchmark for a typical unconventional propeller. The main particulars of the right handed four blades propeller geometry are prescribed in [18] for the model and full scales at which the computation is performed herein. The geometric characteristics of the propeller for the scale ratios of $\lambda = 31.428$ and $\lambda = 1$ are tabulated in Table 1.

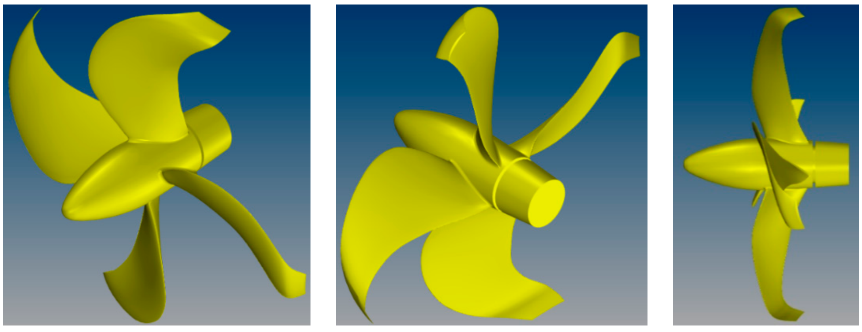

(**a**) (**b**) (**c**)

Figure 1. P1727 propeller geometry. (**a**): pressure side view; (**b**): suction side view; (**c**): side view.

Table 1. Main geometric characteristics of the P1727 propeller.

Parameter	Symbol	UM	Model Scale	Full Scale
Scale ratio	λ	[−]	31.428	1
Propeller diameter	D	[mm]	238.6407	7500.0000
Pitch at r/R = 0.70	$P_{0.7}$	[mm]	200.6109	6304.7994
Pitch at r/R = 0.75	$P_{0.75}$	[mm]	191.0150	6003.2194
Mean pitch	P_{mean}	[mm]	195.4697	6143.2217
Chord length at r/R = 0.70	$c_{0.7}$	[mm]	56.3980	1772.4763
Chord length at r/R = 0.75	$c_{0.75}$	[mm]	55.6172	1747.9374
Thickness at r/R = 0.75	$t_{0.75}$	[mm]	2.9329	92.1752
Pitch ratio at r/R = 0.70	$P_{0.7}/D$	[−]	0.8406	
Mean pitch ratio	P_{mean}/D	[−]	0.8191	
Area ratio	A_{E}/A_0	[−]	0.4438	
Skew	θ_{eff}	[°]	25.6812	
Rake at r/R = 0.70	$\varepsilon_{0.7}$	[°]	−8.9852	
Rake at r/R = 0.75	$\varepsilon_{0.75}$	[°]	−8.8422	
Hub diameter ratio	d_h/D	[−]	0.1542	

The specificity of the propeller considered in the present study is the significant variation of the pitch ratio from the hub to the tip, as Figure 2 shows. As it may be easily observed in the figure, a rather uncommon ε-shaped curve of variation of the pitch in respect to the relative radius makes the propeller be considered as unconventional, see Figure 2a. The variation of the relative chord (*c/D*), thickness (*t/c*) and chamber (*f/c*) in respect to the relative radius is depicted in Figure 2b.

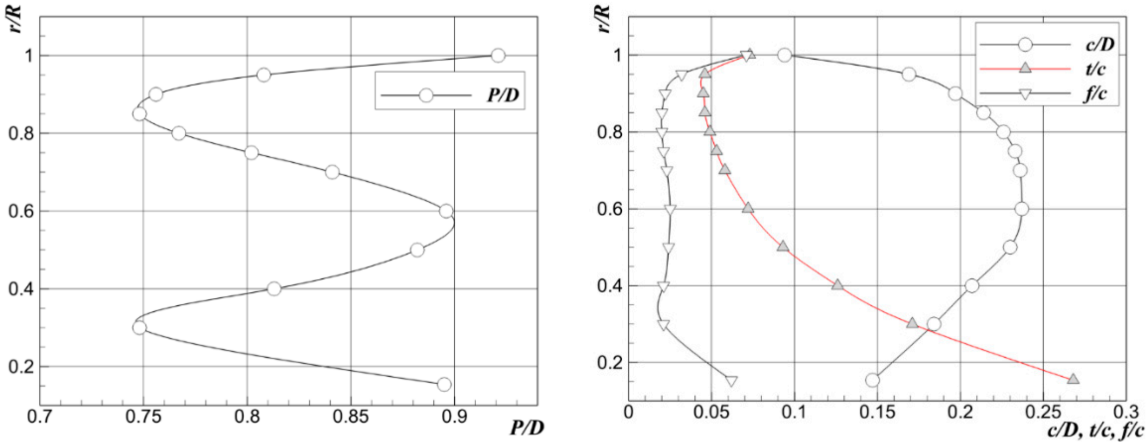

(**a**) (**b**)

Figure 2. Variation of the geometric parameters with the relative radius. (**a**): pitch ratio; (**b**): relative chord, thickness and camber.

2.2. Computational Grid

Let the computational domain be reported to a Cartesian system of coordinates whose origin is located in the geometric center of the propeller, as depicted in Figure 3, which bears out the computational domain and the boundary conditions formulation. The x-axis is oriented towards the downstream, whereas the y and z are the oriented in the lateral and vertical directions, respectively. The domain is of a cylindrical geometry, whose diameter is five times the propeller diameter, while its length is 13.5 times the propeller diameter, out of which 4.25 diameters are at the upstream of the propeller considered as being enough to avoid the influence of the inflow boundary condition imposition on the flow around the propeller. The dimensions of the computational domain fulfilled the minimal conditions imposed by the benchmark computational conditions [18].

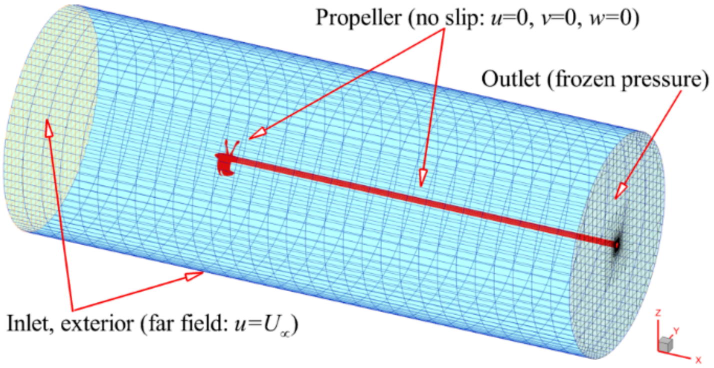

Figure 3. Computational domain and boundary conditions formulation.

The mesh is generated by using the Hexpress component of the FINE™/Marine program (Numeca International, Brussels, Belgium), a generator which has direct CAD import capabilities allowing thus the manipulation or the decomposition of the geometry, a capability which made possible to split the propeller in subsequent sub-surfaces at it will be discussed aftermath. The full automatic hexahedral grid generation is accomplished as the buffer cell and boundary layer insertion for high quality cells in boundary layer regions. The dimensionless wall distance on the propeller blade is chosen such that the viscous sublayer be resolved. Four grids ranging from 7.11 to 59.3 million cells were generated for the purpose of performing the grid convergence test for the solver in the model computational case. In the followings they will be denoted by coarse, medium, fine and very fine, respectively. All the computations are performed on 120 processors, which means that for the finest grid case, a number of about 494,000 cells are computed on each processor. Automatic mesh refinement is performed based on defined sensors next to solid walls. Special attention to the quality criteria such as orthogonality, smoothness and clustering inside the areas next to the solid boundaries is paid during the generation process. Areas of rather heavy clustering are placed around the blade edges and tips, hub and shaft, as Figure 4a–c show.

Figure 4a depicts the grid on the propeller, whereas Figure 4b,c bear out the details of the grid in a longitudinal cut made at $y = 0$ and a cross section made at $x = 0$, respectively. One of the major difficulties to overcome in the present research is represented by the atypical geometry of the propeller at the tips of the blades, where a special attention has to be focused on the mesh generation process. To accomplish this, a special effort is needed by the grid clustering inside that area, where an additional volumetric refinement is imposed. An accurate solution of the viscous flow computation requires a sufficient number of grid cells inside the boundary layer, therefore the local Re number based on the wall variable $y+$ is calculated prior to the grid generation to estimate an appropriate cell size ywall required by the detached eddy simulation (DES hereafter) for the numerical solution setup. Computations performed on the finest grid were based on cells with a thickness of maximum 10^{-6}, so that the $y+$ could be kept below 0.2, as it will be shown in the followings. Obviously, an additional geometric complexity locates inside the region where the dynamometer couples with the hub and the propeller shaft, as shown in Figure 4d where the proper meshing inside the narrow open area may prove the versatility of the HEXPRESS grid generator. Since aside of the forces and moments computations, the present study is also concerned with the intrinsic characteristics of the flow behind the propeller, an additional annular region of rather heavy mesh clustering is placed in the wake for a length of five diameters of the propeller, as depicted in Figure 4e, which shows a longitudinal cut on the computational grid made in the vertical plane of symmetry of the computational domain.

For the full scale computations the finest grid consisting of 71 million cells is generated by imposing the same constraints as for the mesh of the model scale simulation. Since the findings of the grid convergence computations performed on the model are considered as being also valid for the full scale case, no additional grids are generated for the full scale.

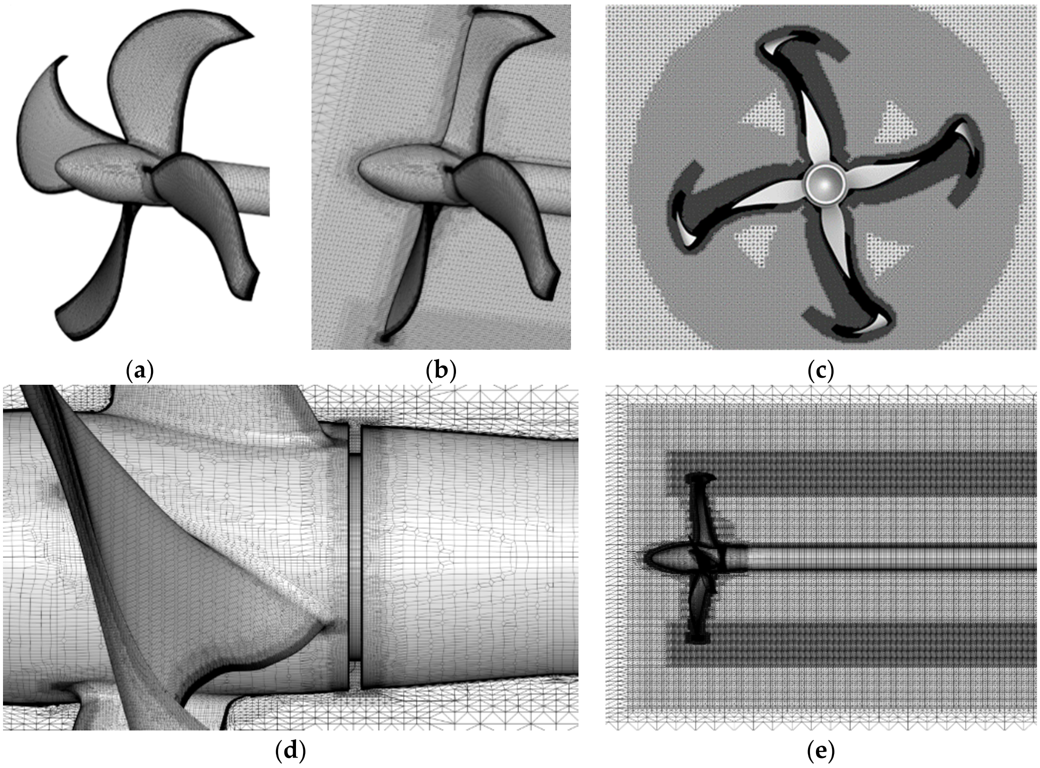
(**a**) (**b**) (**c**)

(**d**) (**e**)

Figure 4. Computational mesh. (**a**): computational mesh on the propeller; (**b**): longitudinal cut on the computational grid; (**c**): cross section on the grid in the geometric center of the propeller; (**d**): detailed view of the grid around the dynamometer clearance; (**e**): grid in the wake of the propeller.

3. Computational Milestones

The ISIS-CFD solver available in the Fine™/Marine package is employed in the present study. The solver is based on the finite-volume method to build the spatial discretization of the transport equations on unstructured grids. The simulation is accomplished in a global approach in which the momentum and mass conservation equations written in respect to a Cartesian system of coordinates are solved. Since no coordinate transformation is done in the solving algorithm, the efficiency of the numerical approach may be considered as being suited to the purpose. Dependent variables of the set of equations are the velocity and pressure.

Closure to the turbulence is achieved through the detached eddy simulation model. Fluxes are built using the AVLSMART bounded difference scheme, which is based on the third order QUICK scheme. Velocity field is obtained from the momentum conservation equation and the pressure field is extracted from the mass conservation constraint transformed into a pressure equation. Picard's procedure is used for the linearization of the equations. The whole discretization is fully implicit in space and time being formally second order accurate. An implicit scheme is applied for the discretization in time whereas a second order three-level time scheme is used for the time-accurate unsteady computation. The turbulence model is using the Shear Stress Transport (SST)-based Detached Eddy Simulation (DES), which provides the accuracy of LES for highly separated flow regions and computational efficiency of RANS in the near-wall region.

The boundary conditions imposed for the simulations reported in here are either Dirichlet or Neumann type. That is, a Dirichlet condition is imposed for the incoming velocity at the upstream and on the exterior boundaries, whereas a Neumann condition in terms of the pressure $(\partial p/\partial n = 0)$ is imposed at the downstream, as shown in Figure 3. The no-slip condition is used on all the solid boundaries. In ISIS-CFD the choice of default free-stream values is: $\omega_\infty = \lambda U_\infty/D$, $\mu_{t\infty} = 10^{-3}\mu_t$, $K_\infty = \mu_{t\infty}\omega_\infty/\rho$ where D is the propeller diameter and U_∞ is the uncomimg velocity at the far inlet. λ is a factor of proportionality, which is recommended to be between 1 and 10. The limits are compatible with values recommended for boundary layer flows, therefore $\lambda = 10$ was chosen [19]. It should be noticed that free-shear layers are more sensitive to small free-stream values of ω_∞ and larger values of ω are recommended in the free-stream: at least $\lambda = 40$ for mixing layers, increasing up to $\lambda = 80$ for round jets. Wall boundary conditions are taken as $K = 0$ and $\omega = 60\mu/\beta\rho(\Delta y)^2$, where Δy is the distance of the first point away from the wall and such that $y^+ < 1$.

When running the code on parallel machines, the computational domain is split into multiple-connected sub-domains having approximately the same number of unknowns. This is done by the METIS partitioning algorithm. Communication of faces data between the sub-domains is performed according to the MPI standard. All the computations are performed on a 624 Intel E5 2680 v3 processors with 12 cores with a frequency of 2.5 GHz and 3.3 GHz for the turbo boost regime. In the very fine mesh computational case, an average of 0.19 millisecond per mesh point was necessary. Each simulation was performed for 25 s, out of which the rotational acceleration time done on a sinusoidal law was one second. 15 to 17 s were sufficient to achieve the convergence of the thrust and torque. During that period the turbulence model is K-ωSST, the time step was 10^{-3} and four iterations were imposed for each time step. After 20 s, the turbulence model is switched to the DES, the time step is decreased to 10^{-5}, whereas the number of iterations per time step was increased to 20. The computation was performed for 5 additional seconds, which were enough for the solution to stabilize.

In the followings, both model and full scale simulations will be considered. All the computations are performed for the non-cavitating regime, at a fixed rate of revolution of 18 revolutions per second (rps) for the model scale computation and of 3.21 rps for the full scale computations. The incoming flow velocity is successively adjusted so that the relative advance ratio be $J = 0.1,\ 0.3,\ 0.5,\ 0.7,\ 0.9$ and the simulations are performed for a water temperature of 15 °C. The computations at the model scale are performed for fresh water, whereas those for the full scale propeller are performed for salt water. The densities of the considered fluids are therefore $\rho = 999\ \mathrm{kg/m^3}$ and $\rho = 1025.97\ \mathrm{kg/m^3}$, respectively.

Simulations at the model scale are conducted under the consideration of laminar-turbulent transition on the blade. For that purpose, a local correlation transition based on the $\gamma - Re_\theta$ model is employed. According to the model, blending together laminar and turbulent flow regimes is achieved by introducing two more transport equations. One is an intermittency equation for γ in which the destruction or re-laminarization term is a function of the vorticity magnitude and ensures that the intermittency remains zero in the laminar boundary layer. The second equation is a transport equation for the local transition onset momentum thickness Reynolds number Re_θ The coupling between the $k - \omega$ SST turbulence model and the transition model [20] is made by an effective intermittency factor y_{eff}, which is used to control the production and destruction terms in the k-equation.

The effective intermittency is defined as $y_{eff} = \max\left(y, y_{sep}\right)$, where y_{sep} is a modified intermittency for predicting separation-induced transition. In the transport equation for k, the production term is multiplied by y_{eff} and the dissipation term is multiplied by $\min\left(\max\left(y_{eff}, 0.1\right),\ 1.0\right)$. The blending function of the model F_1 is also modified in the transition model by adding an extra function that depends on $Re_k = \rho d\sqrt{k}/\mu$, where d is the distance to the wall, is added to the definition of F_1. All the empirical constants of the model are those proposed in [20]. Since the inlet boundary is located four and a half propeller diameters upstream from the propeller reference plane, a decay of the turbulence quantities may occur in the streamwise direction so their values in the propeller region could be different from the inlet boundary. This may raise a question on the appropriateness of the boundary values at the inlet for the transitional flow. Nevertheless, in the present computation such an abnormal behavior has not manifested, therefore no special tunings of the original model were necessary.

For the full scale calculations a fully turbulent inflow is assumed. For the sake of compatibility with the ITTC extrapolation, no special treatment of the propeller surface is made. The thrust and torque of eight different blade sections are evaluated and the total thrust and torque is therefore obtained via the summation of the corresponding blade section values. The coefficients are further subdivided into their pressure and a frictional components to get a more detailed insight into the scale effects on the computed physical parameters.

4. Results and Discussion

4.1. Grid Convergence Test

A series of numerical simulations are discussed in the followings, firstly to perform the grid convergence test, then to carry out the verification and validation of the numerical solutions based on the experimental data (EFD hereafter) provided in [18]. Finally, an analysis of the physical meaning of the computed results for both model and full scales is carried out. A first set of computations is proposed for investigating the grid convergence for the flow around the propeller model. As mentioned before, four different grids tabulated in Table 2 are considered for this purpose. The coarse grid contains 7.11 million cells, the medium one 13.16 million, whereas the fine and the very fine consist of 26.73 and 59.3 million cells, respectively. All the discussions are made only in terms of the thrust and torque coefficients. Because of the restricted available space, the tabulated values of the computed solutions are limited to three decimals only.

Table 2. Grid convergence test. Experimental data from [18].

Parameter		K_T					$10\ K_Q$				
	J	**0.1**	**0.3**	**0.5**	**0.7**	**0.9**	**0.1**	**0.3**	**0.5**	**0.7**	**0.9**
EFD [18]		0.353	0.283	0.209	0.116	0.007	0.39	0.338	0.275	0.181	0.053
CFD	Coarse	0.335	0.269	0.218	0.121	0.007	0.416	0.359	0.259	0.190	0.056
	$\vert\varepsilon\vert\%$	5.181	4.975	4.367	4.117	3.992	6.631	6.129	5.966	5.158	4.877
	Medium	0.369	0.271	0.201	0.120	0.007	0.367	0.356	0.289	0.172	0.055
	$\vert\varepsilon\vert\%$	4.413	4.132	3.972	3.721	3.515	5.816	5.381	5.203	5.016	4.558
	Fine	0.367	0.272	0.216	0.112	0.007	0.410	0.322	0.287	0.188	0.055
	$\vert\varepsilon\vert\%$	4.045	3.881	3.525	3.264	3.013	5.029	4.744	4.415	4.032	1.821
	Very fine	0.360	0.279	0.205	0.114	0.007	0.386	0.340	0.278	0.178	0.052
	$\vert\varepsilon\vert\%$	1.980	1.433	1.911	1.752	1.031	1.026	0.591	1.091	1.870	1.679

As expected, the largest value of the absolute error corresponds to the coarse grid. Errors for K_Q are larger than the corresponding ones for K_T since the torque coefficient is an order of magnitude smaller than the thrust coefficient for a given value of the advance ratio and the numeric representation becomes very important in the computational process. The only exception is represented by the torque coefficients computed on the very fine grid, as shown in Figure 5, which bears out the variation with the cubic root of the number of cells for the four considered grids, $N_C^{1/3}$, of the absolute numerical error $|\varepsilon|$, computed for K_T and $10K_Q$, respectively.

Figure 5a refers to the thrust coefficient, whereas Figure 5b to the torque coefficient. The reason for reporting the errors to the cubic root of the cell numbers resides on the fact that when using an unstructured mesh, it is difficult to define a parameter that may describe locally the accuracy of the fineness of the discretization. Figure 5 shows that the trend of the numerical error is to decrease with the increase of the accuracy of the discretization, as expected. In spite of its monotonic decrease trend, the slopes of the curves vary with the number of the cells. Although this behavior may not represent a crucial drawback of the numerical simulation, more computational trials are obviously required to get a deeper insight into the reasons of its occurrence.

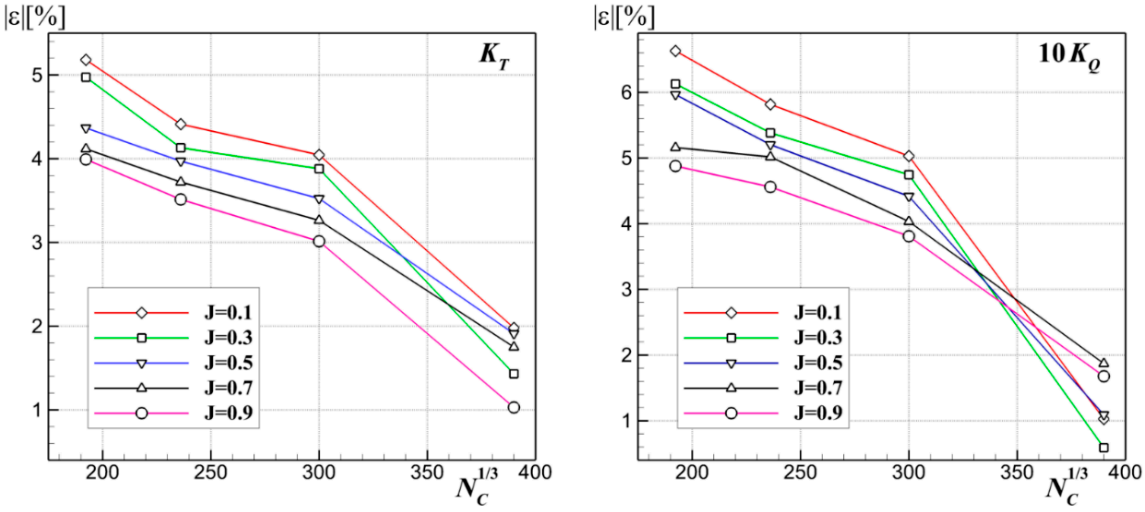

(**a**) (**b**)

Figure 5. Computational error versus the cubic root of the cell number (N_C). (**a**): K_T; (**b**):$10K_Q$.

4.2. Overall Performances of the Model and Full Scale Propellers

With the grid convergence test at hand, for obvious reasons, only the solutions computed on the very fine grid will be considered in the followings. As it has been already proven, the best way of validating a numerical solution still remains the validation through comparisons with experimental data, whenever they exist. For that purpose, a comparison between the computed propeller performance curves and the corresponding measured ones [18] is proposed in Figure 6a for the five advance ratio coefficients imposed by the ITTC benchmark. According to the values related to the finest grid tabulated in Table 2, a satisfactory good resemblance can be emphasized, a fact that may suggest not only the accuracy of the numerical method employed, but also the robustness of the solver, as proven by the author in previous studies [21,22].

The solutions computed on the model scale are in a good agreement with most of those reported in [18], where various solvers were used by the 13 participants engaged in solving the ITTC 2018 Propulsion Committee benchmarking problem. However, contrary to the concluding remarks of the final report [18], which noticed that the numerical solutions reported by the participants underestimated the thrust and torque coefficients, the solutions presented here do not show the same tendency, as Figure 6a and Table 2 prove. The better accuracy of the present solution may be attributable to the mesh resolution on the propeller blade, which is about four times higher than the finest grid used by the reporters in [18]. This fact may suggest that a proper accuracy may only be achieved on a grid of a good quality. It is worth mentioning that none of the reporters in [18] used the DES model to get closure to turbulence, therefore the author believes that a merit may also have the turbulence model employed in here. Previous comparative studies performed either by the author [21,22] based on the K-ω SST and EASM turbulence models or by the group involved in the solver development [23] proved that DES model is providing the most accurate solutions in spite of the increased associated computational costs.

Next, a comparison between the thrust and torque coefficients computed and extrapolated according to the ITTC'78 methodology on the full scale propeller is proposed in Table 3. Again the largest errors correspond to the highest advance ratio coefficient, seemingly due to the round-off errors, as explained above. A similar conclusion can be withdrawn from Figure 6b, which reveals a similar underestimation of the efficiency, as reported in [18].

Table 3. Comparison between the thrust and torque coefficients computed and extrapolated according to ITTC'78 procedure for the propeller at full scale.

Coefficient	***J*** **[−]**	***J* = 0.1**	***J* = 0.3**	***J* = 0.5**	***J* = 0.7**	***J* = 0.9**
K_T	ITTC '78	0.353	0.284	0.209	0.117	0.008
	CFD	0.359217	0.280827	0.209459	0.114963	0.007707
	$\lvert\varepsilon\rvert\%$	1.731	1.12	0.219	1.772	3.802
$10\ K_Q$	ITTC '78	0.383	0.332	0.269	0.174	0.046
	CFD	0.387532	0.342681	0.275096	0.175402	0.047744
	$\lvert\varepsilon\rvert\%$	1.169	3.117	2.216	0.799	3.653

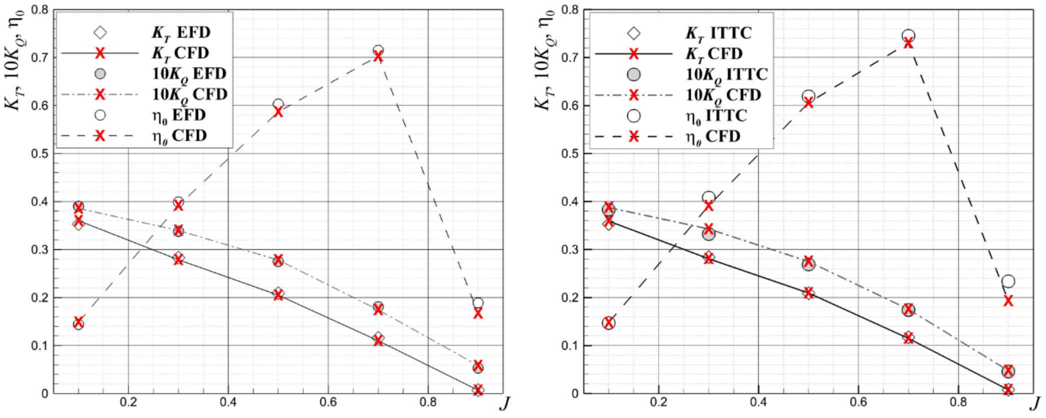

(**a**) (**b**)

Figure 6. Comparison between the performance curves for the P1727 propeller: (**a**): computed and measured at model scale, provided in [18]; (**b**): computed for the full scale.

The grid uncertainty was computed using the methodology described in [24] for monotonic convergence. In the followings a verification and validation of the computed thrust coefficient K_T will be described only for $J = 0.9$ case, which produced the smallest error compared to the experimental data. The grid ratio (r_G), the associated relative error between the K_T computed on the finest mesh $M4$ and the second finest mesh $M3$, $\varepsilon_{43}\%K_{T4}$, the ratio between the estimated order of convergence and the theoretical order of convergence p_G/p_{Gth}, the grid uncertainty $U_G\%M_4$, the experimental uncertainty $U_D\%D$ and the validation uncertainty $U_v\%$ are tabulated in Table 4. $p_{G,th}$ in Table 4 is the theoretical order of accuracy, which is the order of convection scheme, whereas the validation uncertainty is $U_V = \sqrt{(U_G\%M_4)^2 + (U_D\%D)^2}$. The relative error between the solution computed on the finest mesh $M4$ and the experimental data for the thrust coefficient is smaller than the Richardson-based validation numerical uncertainty, therefore the K_T prediction can be considered as being validated. Similar conclusion can be withdrawn for K_Q.

Table 4. Verification and validation for the thrust coefficient computed at the model scale for $J = 0.9$.

Parameters	r_G	$\varepsilon_{43}\%K_{T4}$ **or** $\varepsilon_{43}\%K_{Q4}$	$p_G/p_{G,\,th}$	$U_G\%M_4$	$U_D\%D$	$U_V\%$
K_T	2.023	1.982	1.023	1.791	1.0	2.051
$10\ K_Q$	2.023	0.142	1.023	1.791	1.0	2.051

The distribution of forces and moments on the propeller blades is further analyzed on a sectorial basis to clarify which of their local components are influenced the most by the scale effects. For that purpose, the pressure and frictional thrust and torque on eight circular sectors of the propeller, are computed and the results are tabulated in Tables A1–A5 in Appendix A, where the subsequent distribution of the coefficients computed for the propeller model and their total values are given. Each table refers to a particular advance coefficient. Similarly, the pressure and frictional forces and moments are computed on each sector for the full scale propeller on the same eight circular sectors, as tabulated in Table A6, Table A7, Table A8, Table A9, Table A10 given in Appendix B. The sectors extend from the hub to the tip and they are of uneven widths. The numerical solutions are depicted in Figure 7, which shows the radial distribution of the total thrust coefficients computed in the model and full scale operating flow conditions. Computed values are represented in the center of each sector. The largest values of the thrust correspond to sectors located between $r/R = 0.8$ and $r/R = 0.9$.

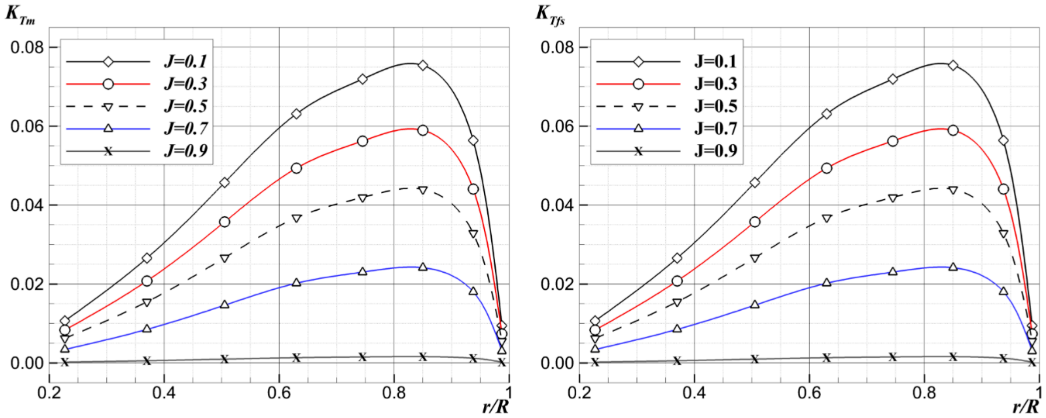

(**a**) (**b**)

Figure 7. Radial distributions of the computed thrust coefficients. (**a**): model scale; (**b**): full scale.

The solutions tabulated in the tables of Appendix A show that the average pressure component is the most significant share of the thrust coefficient for the lower advance ratios. For heavier loadings the percentage of the pressure coefficient decreases monotonically form 98.1% to 88.98%, with the largest value corresponding to the smallest advance ratio. However, for the $J = 0.9$ case, the pressure component participation in the total budget of the thrust coefficient drops to only 54.06%, seemingly due to the low streamwise incoming velocity of the flow. About same conclusions can be withdrawn if the full scale solutions are analyzed. The monotonic decrease of the thrust coefficient is also manifested by the torque coefficient that varies from 91.8% at $J = 0.1$ to 85.42% at $J = 0.7$, then drops to 64.7% for $J = 0.9$. The same conclusions may be drawn from Figure 8, which depicts a comparison for the torque coefficients computed for the two working regimes.

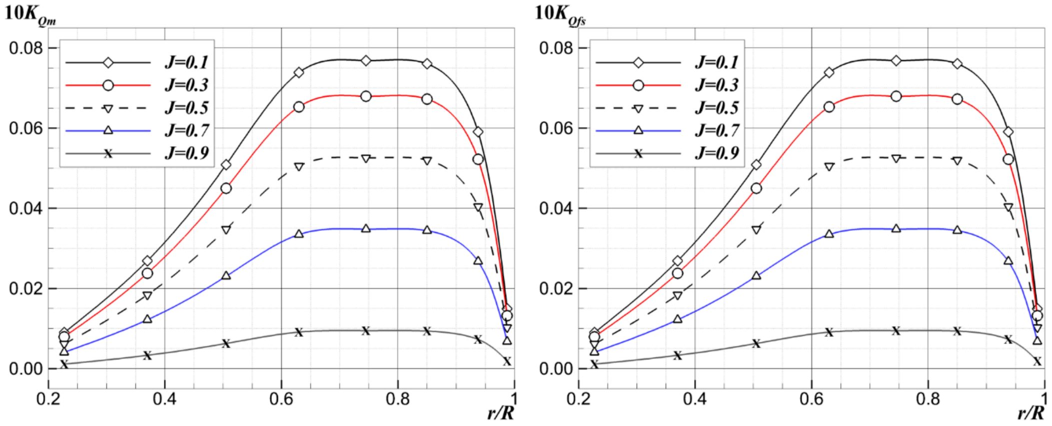

(**a**) (**b**)

Figure 8. Radial distribution of the computed torque coefficients. (**a**): model scale; (**b**): full scale.

Sizing the existing differences between the corresponding numerical solutions for the model and full scale computations based on Figures 7 and 8 only might be difficult for the reader, so they will be analyzed separately in Figure 9. Obviously, the largest differences correspond to the sectors located between $r/R = 0.63$ and $r/R = 0.85$ where the thrust and torque coefficients have the largest values. They represent 2.198% for K_T computed at $J = 0.5$ and 1.701% for $10K_Q$ computed at $J = 0.7$. In terms of the average differences computed for the entire propeller, they have a maximum of 1.831% for K_T, which corresponds to $J = 0.5$, and 1.312% for $10K_Q$ computed at $J = 0.7$. Based on these figures it may be concluded that the transposition from the model scale to the full scale solutions did not introduce significant errors since the discretization in space and time is sufficiently good and the numerical setup was done properly. In spite of the accuracy of the solutions, considering the cost associated to the CPU time spent for such a simulation, it may be raised a doubt whether such a detailed study may be a choice for a regular daily use or not, especially when fast technical decisions are expected.

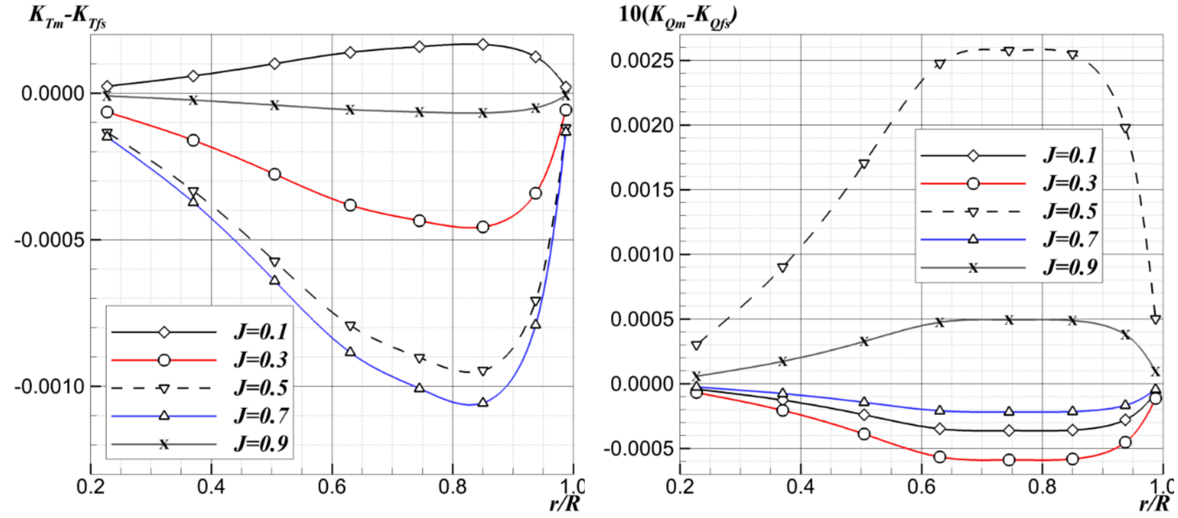

(**a**) (**b**)

Figure 9. Radial distribution of the differences between the thrust and torque coefficients computed at model and full scales. (**a**): Model scale; (**b**): full scale.

4.3. *Characteristics of the Local Flow around the Model and Full Scale Propellers*

Although it did not represent a required task of the ITTC 2018 benchmarking, the present study will present some intrinsic particulars of the local flow around the two propellers considered. The objective of the proposed introspection is to assess not only the proposed methodology, but also the numerical schemes behind it as well as to identify the limitations of the method. The analysis is performed separately for the two propellers considered. For the sake of similarity, the comparisons are made on the solutions computed for $J = 0.9$ only and refer to the same physical parameters of the flow. A special attention will be paid to the flow structure in the wake of the propeller since its structure may offer the needed clarifications on the design performances as well as on its eventual drawbacks.

4.3.1. Model Scale Propeller

At first, an analysis of the vortical structures developed in the wake of the propeller is proposed in Figure 10, which shows the isosurfaces of the dimensionless second invariant of the velocity gradient computed for $J = 0.9$, $J = 0.7$ and $J = 0.5$, respectively.

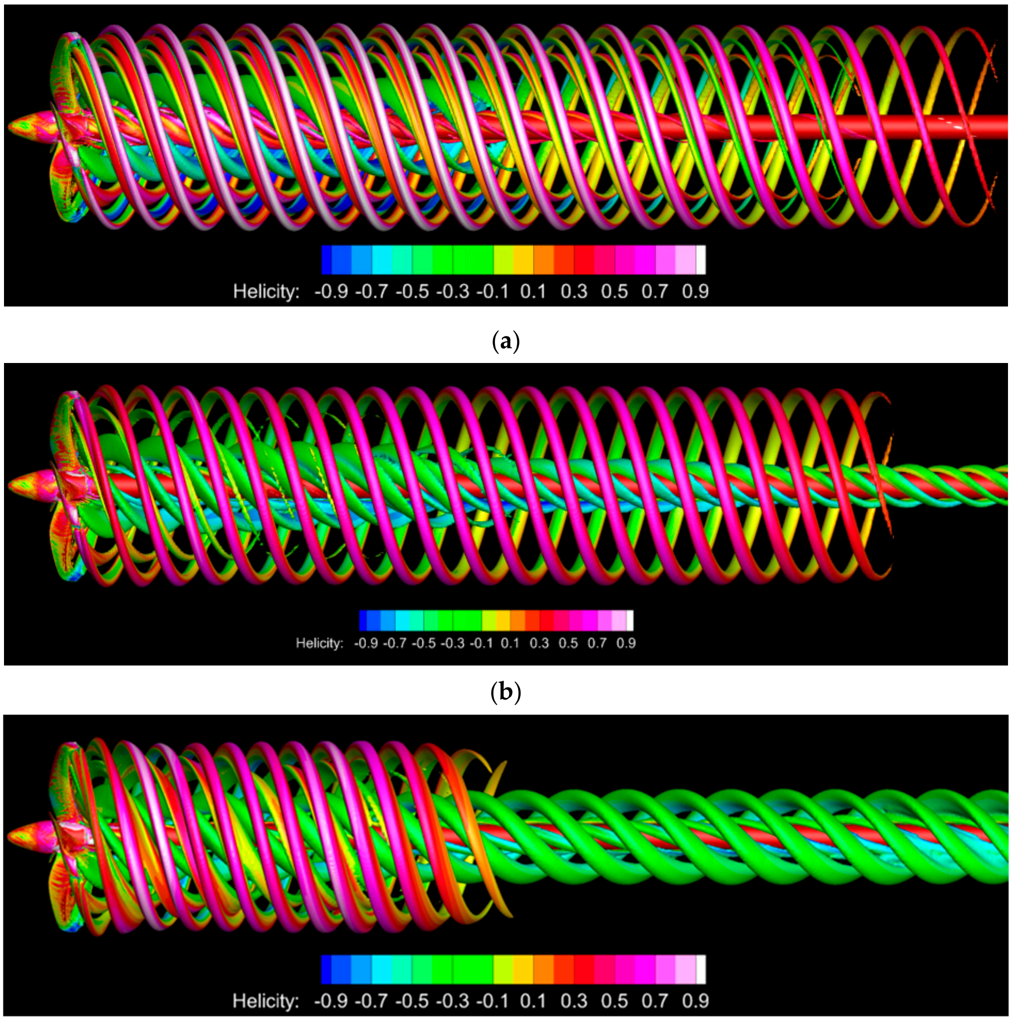

(**a**)

(**b**)

(**c**)

Figure 10. Comparison between the vortical structures in the wake of the propeller model computed at different advance ratios. (**a**): $J = 0.9$; (**b**): $J = 0.7$; (**c**): $J = 0.5$.

The isosurfaces of the second invariant are colored by helicity. The second invariant of the velocity gradient can be expressed as $Q = 0.5 \cdot \left(\Omega_{ij}\Omega_{ij} - S_{ij}S_{ij}\right)$, where $S_{ij} = \left(U_{ij} + U_{ji}\right)/2$ is the symmetric part (rate of strain) whereas $\Omega_{ij} = \left(U_{ij} - U_{ji}\right)/2$ is the non-symmetric part (rate of rotation). U in the equations above is the oncoming flow velocity. A vortex core is located where the Q invariant is positive and the local pressure has a lower value than the ambient.

Although the trajectories of the tip vortices in the longitudinal plane remain almost constant in the wake at high aspect ratios, they slightly incline towards the shaft on the whole, suggesting a contraction, which becomes more significant as the advance ratio decreases. Obviously, the load conditions affect substantially both hub vortex and tip vortices. This can be seen in Figure 10c, which depicts the vortices released by the propeller at $J = 0.5$. The intensity of the tip vortices is getting weaker far in the wake, a fact which is seemingly due to the viscous interaction with the rest of the fluid.

With the increase of the downstream distance, the propeller trailing vortex restores gradually to the free-stream flow and the fluctuation of the circumferential distribution of axial velocities becomes weaker. The helical pitch of the vortices is constant, a fact that suggests that no numerical dissipation takes place. This is a merit of the solver, which indicates suitable conservation properties and of the heavy clustering of the mesh at the downstream of the tips, which proves to be non-dissipative.

To explain the vortex generation mechanism, a longitudinal cut in the downstream vortical field is proposed in Figure 11, which reveals three types of vortices, depending on the place of their formation.

Tip vortices denoted by "A" in the figure cohabitate with the root ones, i.e., "B" vortices as well as with the ones generated by the sharp edges of the dynamometer clearance, which lay along the shaft and denoted by "C" in the figure. Aside of that, in the immediate vicinity of the propeller, a weaker set of secondary set of three vortices is released by the blade tips and eventually vanishes because of the weaker intensity. Although the present propeller is of an unconventional geometry, the mechanism is similar to that reported by the author in [19] where the KP505 five-bladed propeller was analyzed.

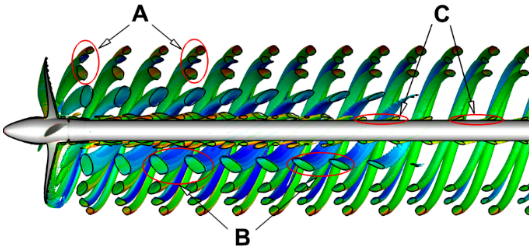

Figure 11. Mechanism of vortical structure formation and evolution.

Next, the flow kinematics and turbulence parameters will be analyzed. Figure 12 displays the contours drawn in the longitudinal plane of $y = 0$ of the propeller model for: (a) the non-dimensional streamwise velocity; (b) vorticity; (c) turbulent kinetic energy and (d) turbulent viscosity. The wake dynamics is mainly dominated by the tip and hub vortices, as Figure 12a bears out. Both axial velocity and vorticity manifest periodic pulses that correspond to the cores of the vortices. Their intensity decreases in the downstream because of the viscous dissipation, as depicted in Figure 12a,b. Strong tip-released structures are shed in the wake, correlating with local maxima of turbulent kinetic energy. Nevertheless, they are not a long standing feature of the propeller wake. In contrast, helical structures originating from the root of the propeller blades are more persistent and their footprint is still visible few propeller diameters downstream. Computations proved that for increasing loads, turbulent kinetic energy experiences a faster growth at the wake axis, populated by the hub vortex, compared to the outer radii, dominated by the tip vortices, see Figure 10c. The evolution of turbulent kinetic energy at the outer edge of the wake is not monotonic, in contrast with that inside the core placed around the shaft, due to mutual interaction and associated shear between tip vortices and the wake of the neighboring blades.

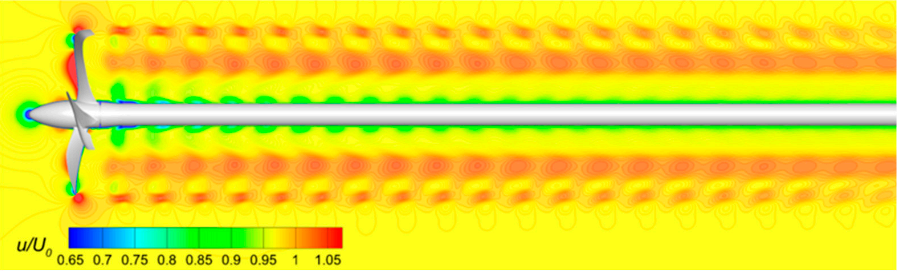

(**a**)

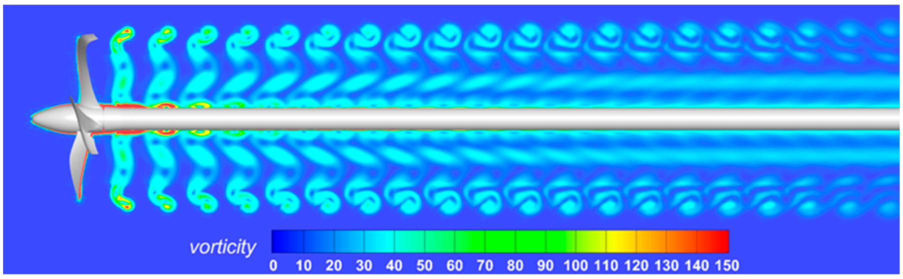

(**b**)

Figure 12. *Cont.*

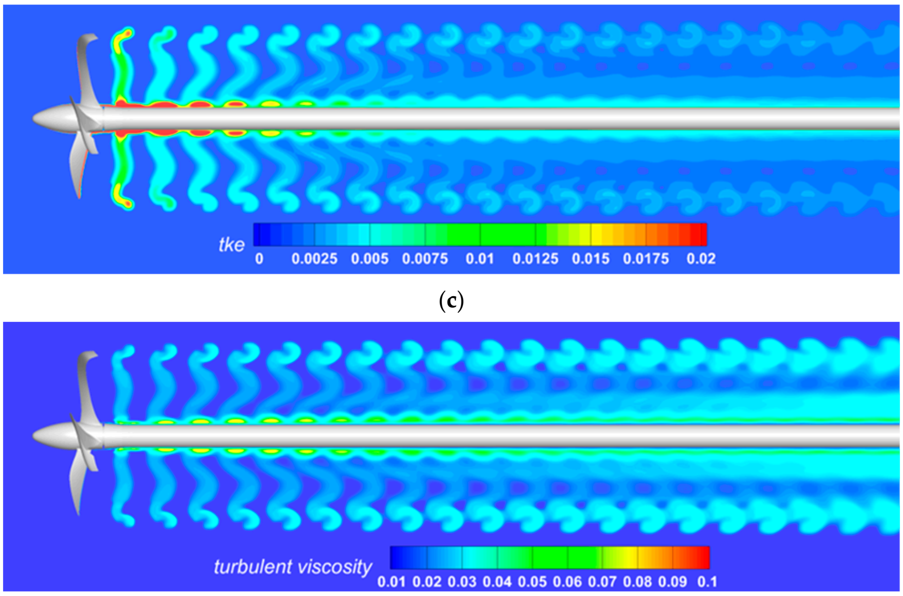

(**c**)

(**d**)

Figure 12. Longitudinal distribution of the main parameters of the flow in the symmetry plane of the propeller model, computed at $J = 0.9$. (**a**): non-dimensional axial velocity; (**b**): vorticity; (**c**): turbulent kinetic energy; (**d**): turbulent viscosity.

As mentioned before, the overall accuracy of the numerical solution is highly dependent not only on the numerical scheme but also on the quality of the discretization. In spite of the rather low efficiency because of the CPU costs, the present study has been performed on a mesh whose density was high enough to assure a low y^+ everywhere on the solid surface, so that the DES model could work properly. This can be seen in Figure 13, which shows the distribution of the non-dimensional distance y^+ on the propeller model.

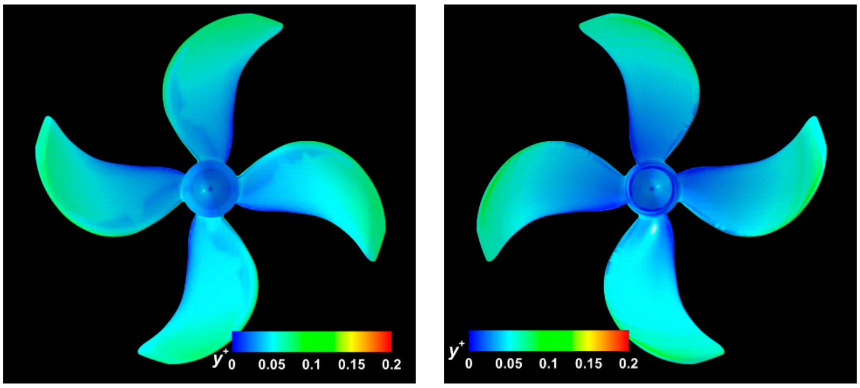

(**a**) (**b**)

Figure 13. y^+ distribution on the propeller model computed for $J = 0.5$. (**a**): pressure side; (**b**): suction side.

Next, a comparison of the non-dimensional axial velocity fields computed in three different cross-section is proposed in Figure 14. The transversal cuts are made in the propeller plane, Figure 14a, at $x = 0.5\ R$ and $x = \mathrm{R}$ in Figure 14b,c, respectively. Obviously the streamwise velocity reaches a maximum in the propeller plane, then it decreases with an average of about 10% every half of the radius, seemingly because of the viscous dissipation.

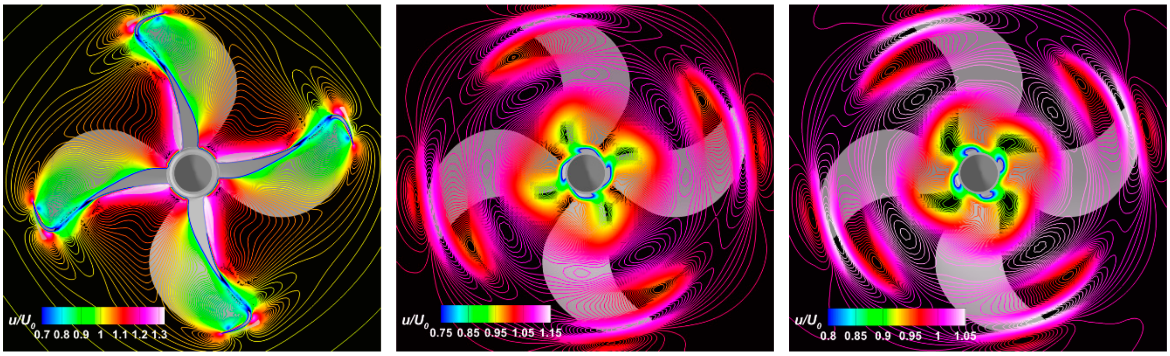

(**a**) (**b**) (**c**)

Figure 14. Transversal distribution of the non-dimensional streamwise velocity computed for $J = 0.9$. (**a**): $x = 0$; (**b**): $x = 0.5\ R$; (**c**): $x = R$.

4.3.2. Full Scale Propeller

Computing the flow at the full scale has some particularities, which are mostly determined by the different *Re* number at which the simulations are performed. Although apparently tempting, the computational mesh for the full scale cannot be generated via an unsophisticated multiplication of node coordinates from the model scale by an elementary scaling. Generally speaking, surface elements on the solid walls of the propeller and volumetric elements of the major part of the computational domain can be scaled in this way, but a straightforward scaling of dimensions of the cells composing the boundary layer is not correct since the relative thickness of the boundary layer decreases with the increasing *Re* number.

Wishing to keep the mesh size at a reasonable level, the refinement in the wake could not be possible as for the model scale computations, i.e., only three and a half diameters, comparing to the five diameters imposed in the model scale computation. Knowing that a rough discretization acts as a numerical damper, the author believes that this is the main reason of heaving the solutions depicted in Figures 15 and 16 not propagating sufficiently in the wake of the propeller.

Regardless of that, it is worth to underline that the helical pitch of the vortices remains constant, as in the model scale computations. Since all the discussions above based on the model case solution remain valid here, no special assertions will be made on the solutions computed on the propeller at the full scale. For the sake of similarity, the same analysis is proposed for the main kinematic and dynamic parameters that describe the flow in Figures 16 and 17, so that the differences between the two cases may be conveniently emphasized. One of the most obvious difference is that all the physical parameters drawn in Figure 16 manifest a stronger decay in the downstream region of the full scale propeller compared to those drawn in Figure 12 at model scale. One of the reasons is that the full scale computation is performed for the propeller working in salt water, therefore at a different Reynolds number. Moreover, the computation at the model scale is based on the assumption of the transition from the laminar model to turbulence, whereas at the full scale the flow is assumed to be fully turbulent. Obviously, the differences may also be attributable to the different grids that were used in the simulations, as explained above. Figure 17 shows the non-dimensional streamwise velocity fields drawn in three cross-sections drawn at the same relative positions in respect to the propeller plane as in Figure 14. Comparing the two figures, it may be pointed out that excepting the region placed behind the trailing edges of the blades at around $r/R = 0.6$, where rather strong gradients of velocity were present in the model case solution, their intensity at full scale is lower because of the stronger dissipation that takes place there.

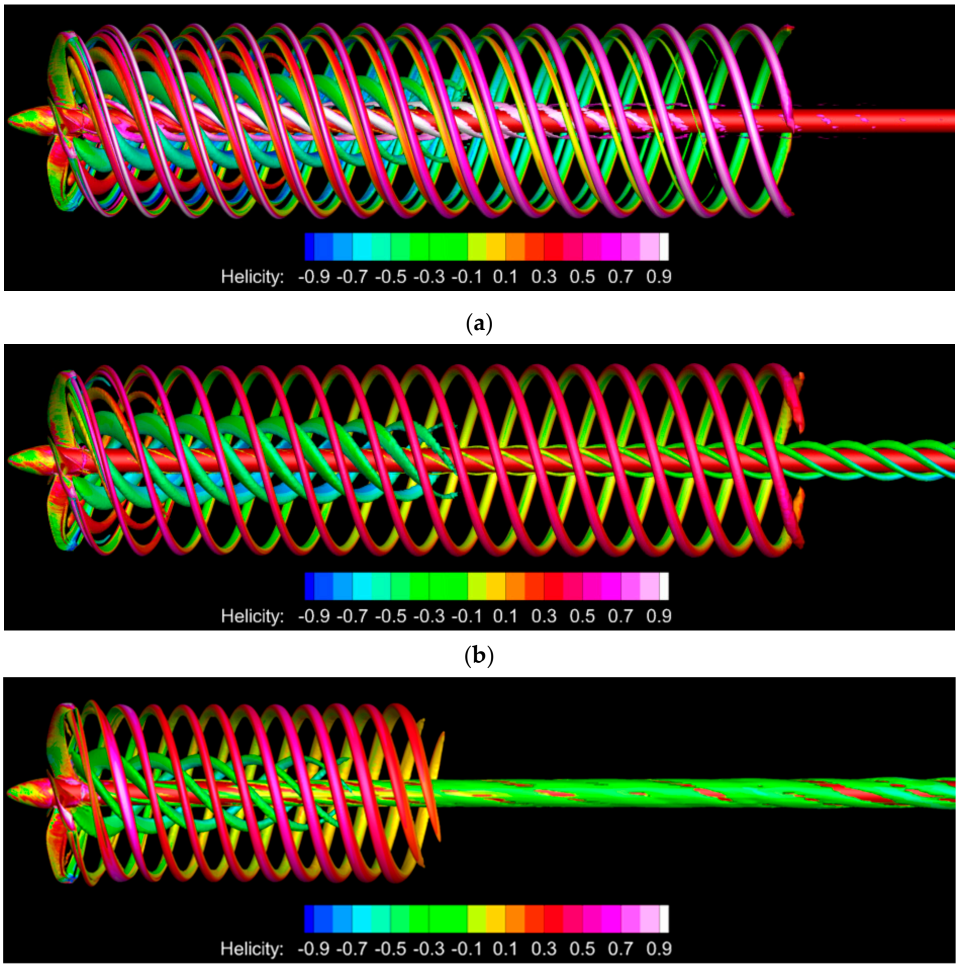

(**a**)

(**b**)

(**c**)

Figure 15. Comparison between the vortical structures in the wake of the full scale propeller computed at different advance ratios. (**a**): $J = 0.9$; (**b**): $J = 0.7$; (**c**): $J = 0.5$.

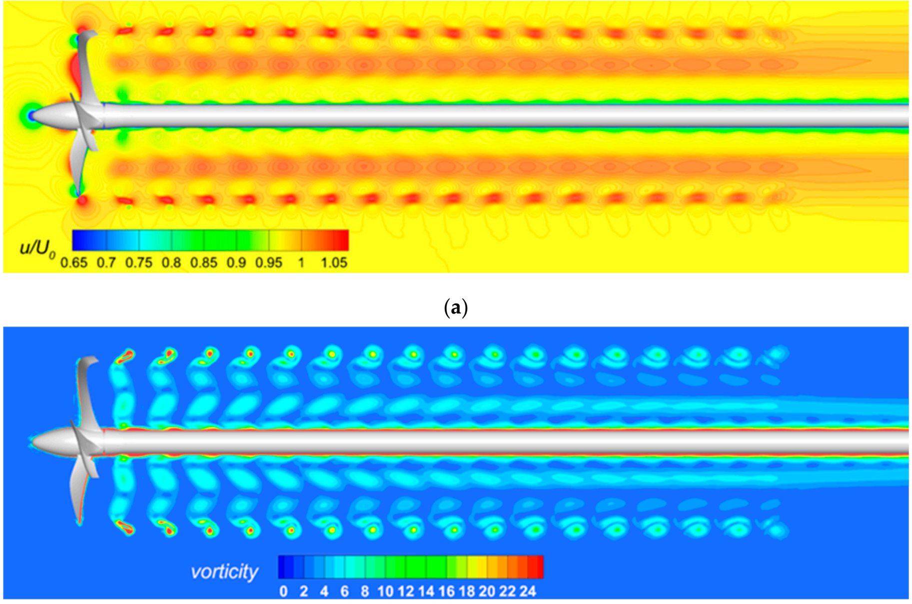

(**a**)

(**b**)

Figure 16. *Cont.*

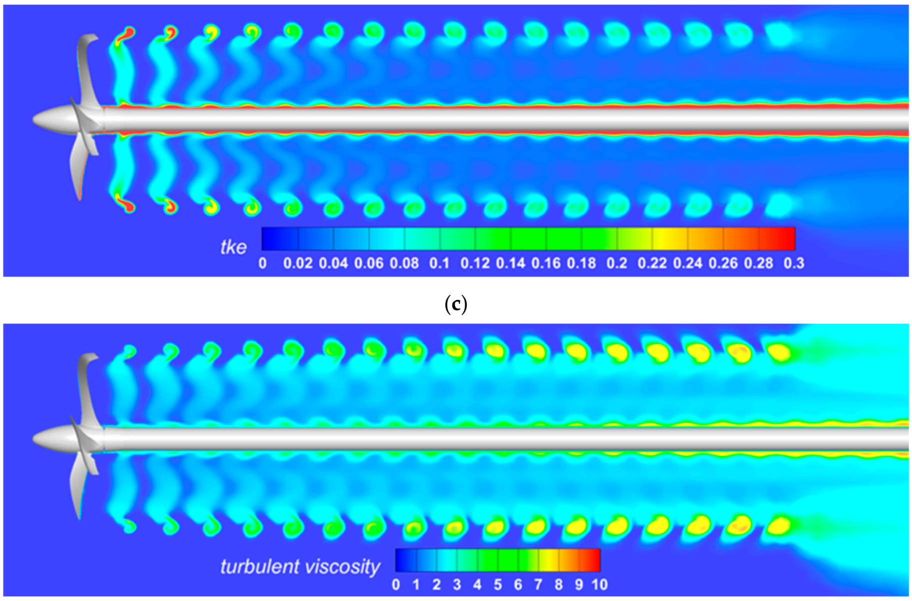

(**c**)

(**d**)

Figure 16. Longitudinal distribution of the main parameters of the flow in the symmetry plane of the full scale propeller. (**a**): streamwise velocity; (**b**): vorticity; (**c**): turbulent kinetic energy; (**c**): turbulent viscosity.

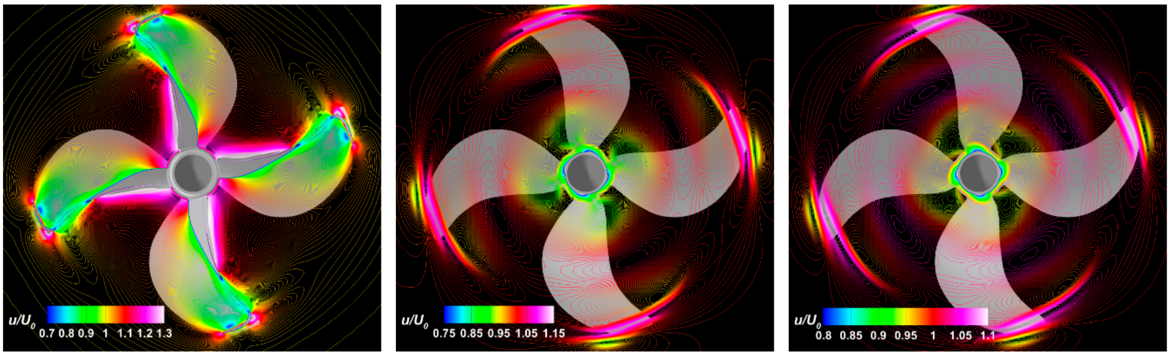

(**a**) $x = 0$ (**b**) $x = 0.5\ R$ (**c**) $x = R$

Figure 17. Transversal distribution of the non-dimensional streamwise velocity computed for $J = 0.9$. (**a**): $x = 0$; (**b**): $x = 0.5\ R$; (**c**): $x = R$.

5. Concluding Remarks

Scale effects on the open water characteristics of an unconventional propeller have been numerically investigated by using the ISIS-CFD solver of the Fine™/Marine software package in which closure to turbulence was achieved through the DES model. The DES model allows a better capturing of the vortical structures that develop in the propeller wake. This is important not only for the correct estimation of the pressure fluctuations induced by the propeller working behind a ship hull on the overhang structure, but also for the underwater propeller noise propagation, which is critical for the navy ships. Aside of that, a proper velocity and pressure estimation is of a great help for an accurate estimation of the forces and moments that act not only on the bearings of the shaft line, but also on the rudder, with consequences on the maneuverability performances. Wrapping up, a better treatment of the turbulence by making use of DES or LES models may offer more comprehensive information, but for higher simulation costs.

A local correlation transition based on the $\gamma - Re_\theta$ model was employed to simulate the transition to the turbulence. All computations were performed by resolving the boundary flow down to the wall, without making use of wall functions. The P1727 propeller geometry and the flow conditions were those prescribed by SVA Potsdam as the 28th ITTC Propulsion Committee benchmark. Following a grid convergence test performed on four meshes, parallel computations at model and full scale were carried out for five advance ratio coefficients and the numerical solutions were compared to the experimental data to validate the theoretical approach. Wrapping up all those discussed before, the following remarks may be put forward:

(a) the mean dimensionless wall distances on the propeller blades was kept smaller than $y^+ < 0.2$ at model scale;
(b) the highest thrust of the propeller is generated by the radial section between $0.8 < r/R < 0.9$;
(c) the thrust and torque coefficients computed at model scale agree well with the experimental data;
(d) the agreement between the computed full-scale thrust coefficients with the extrapolated values according to the ITTC'78 method is more than satisfactory;
(e) the numerical simulation at the full scale can be successfully used in the design process if the solution is based on a careful discretization of the computational domain, as well as on a proper choice of the numerical scheme.

Funding: This research received no external funding.

Acknowledgments: The author acknowledges the generosity of Ulf Barkmann, deputy head of the Department Propeller & Cavitation at the Schiffbau-Versuchsanstalt Potsdam GmbH, which kindly provided the experimental data needed for the comparisons contained in the present research.

Conflicts of Interest: The author declares no conflict of interest.

Appendix A

Appendix A contains the tabulated thrust and torque coefficients decomposed into their frictional $\left(K_{Tf},\ 10K_{Qf}\right)$ and pressure $\left(K_{Tp},\ 10K_{Qp}\right)$ components, computed for the propeller model on eight radial sectors of the blades between the hub and the tip of the propeller. In addition, the tables contain the total value of the coefficients, which are obtained by summing up the sectorial values. The position of the center of each sector is specified in the *r/R* column.

Table A1. Radial distribution of the propeller coefficients computed for $J = 0.1$ at model scale.

$\Delta r/R = (r/R)_i – (r/R)_{i-1}$	r/R	K_{Tf}	K_{Tp}	K_T	$10K_{Qf}$	$10K_{Qp}$	$10K_Q$
d_h–0.30	0.2271	0.000200	0.010477	0.010677	0.000736	0.008191	0.008927
0.30–0.44	0.3700	0.000500	0.026136	0.026636	0.002208	0.024577	0.026785
0.44–0.57	0.5050	0.000859	0.044951	0.045810	0.004172	0.046449	0.050622
0.57–0.69	0.6300	0.001186	0.062076	0.063262	0.006060	0.067463	0.073522
0.69–0.80	0.7450	0.001352	0.070726	0.072078	0.006304	0.070186	0.076490
0.80–0.90	0.8500	0.001418	0.074171	0.075589	0.006238	0.069444	0.075682
0.90–0.975	0.9375	0.001060	0.055443	0.056503	0.004846	0.053955	0.058802
0.975–1.00	0.9875	0.000177	0.009277	0.009455	0.001226	0.013647	0.014873
Σ		0.006752	0.353257	0.360009	0.031790	0.353913	0.385702

Table A2. Radial distribution of the propeller coefficients computed for $J = 0.3$ at model scale.

$\Delta r/R = (r/R)_i – (r/R)_{i-1}$	r/R	K_{Tf}	K_{Tp}	K_T	$10K_{Qf}$	$10K_{Qp}$	$10K_Q$
d_h–0.30	0.2271	0.000201	0.008063	0.008264	0.00069	0.007175	0.007862
0.30–0.44	0.3700	0.000501	0.020116	0.020617	0.00206	0.021530	0.023591
0.44–0.57	0.5050	0.000862	0.034596	0.035458	0.00389	0.040691	0.044586
0.57–0.69	0.6300	0.001190	0.047776	0.048966	0.00566	0.059099	0.064756
0.69–0.80	0.7450	0.001356	0.054434	0.055790	0.00589	0.061485	0.067370
0.80–0.90	0.8500	0.001422	0.057085	0.058507	0.00582	0.060835	0.066658
0.90–0.975	0.9375	0.001063	0.042672	0.043734	0.00452	0.047266	0.051790
0.975–1.00	0.9875	0.000178	0.007140	0.007318	0.00114	0.011955	0.013099
Σ		0.006771	0.271883	0.278654	0.029676	0.310038	0.339713

Table A3. Radial distribution of the propeller coefficients computed for J = 0.5 at model scale.

$\Delta r/R = (r/R)_i – (r/R)_{i-1}$	r/R	K_{Tf}	K_{Tp}	K_T	$10K_{Qf}$	$10K_{Qp}$	$10K_Q$
d_h–0.30	0.2271	0.000216	0.005996	0.006212	0.000612	0.005524	0.006135
0.30–0.44	0.3700	0.000539	0.014958	0.015497	0.001835	0.016574	0.018409
0.44–0.57	0.5050	0.000927	0.025726	0.026653	0.003468	0.031324	0.034793
0.57–0.69	0.6300	0.001280	0.035527	0.036807	0.005037	0.045495	0.050532
0.69–0.80	0.7450	0.001458	0.040478	0.041936	0.005241	0.047332	0.052572
0.80–0.90	0.8500	0.001529	0.042450	0.043979	0.005185	0.046832	0.052017
0.90–0.975	0.9375	0.001143	0.031731	0.032874	0.004029	0.036386	0.040415
0.975–1.00	0.9875	0.000191	0.005310	0.005501	0.001019	0.009203	0.010222
Σ		0.007125	0.197828	0.204953	0.027721	0.250367	0.278089

Table A4. Radial distribution of the propeller coefficients computed for J = 0.7 at model scale.

$\Delta r/R = (r/R)_i – (r/R)_{i-1}$	r/R	K_{Tf}	K_{Tp}	K_T	$10K_{Qf}$	$10K_{Qp}$	$10K_Q$
d_h–0.30	0.2271	0.000374	0.003016	0.003390	0.000588	0.003446	0.004034
0.30–0.44	0.3700	0.000932	0.007524	0.008456	0.001764	0.010340	0.012104
0.44–0.57	0.5050	0.001603	0.012940	0.014543	0.003335	0.019542	0.022877
0.57–0.69	0.6300	0.002214	0.017870	0.020084	0.004843	0.028383	0.033226
0.69–0.80	0.7450	0.002522	0.020361	0.022883	0.005039	0.029528	0.034567
0.80–0.90	0.8500	0.002645	0.021352	0.023997	0.004985	0.029216	0.034202
0.90–0.975	0.9375	0.001977	0.015961	0.017938	0.003873	0.022700	0.026573
0.975–1.00	0.9875	0.000331	0.002671	0.003002	0.000980	0.005741	0.006721
Σ		0.008234	0.101695	0.114293	0.025408	0.148896	0.174304

Table A5. Radial distribution of the propeller coefficients computed for J = 0.9 at model scale.

$\Delta r/R = (r/R)_i – (r/R)_{i-1}$	r/R	K_{Tf}	K_{Tp}	K_T	$10K_{Qf}$	$10K_{Qp}$	$10K_Q$
d_h–0.30	0.2271	0.000092	0.000109	0.000201	0.000428	0.000784	0.001211
0.30–0.44	0.3700	0.000231	0.000271	0.000502	0.001283	0.002352	0.003635
0.44–0.57	0.5050	0.000397	0.000467	0.000864	0.002425	0.004444	0.006870
0.57–0.69	0.6300	0.000548	0.000645	0.001193	0.003522	0.006455	0.009978
0.69–0.80	0.7450	0.000624	0.000735	0.001359	0.003665	0.006716	0.010380
0.80–0.90	0.8500	0.000655	0.000770	0.001425	0.003626	0.006645	0.010271
0.90–0.975	0.9375	0.000489	0.000576	0.001065	0.002817	0.005163	0.007980
0.975–1.00	0.9875	0.000082	0.000096	0.000178	0.000713	0.001306	0.002018
Σ		0.003117	0.003669	0.006787	0.024371	0.033864	0.052343

Appendix B

Similar to Appendix A, Appendix B contains the tabulated thrust and torque coefficients decomposed into their frictional $\left(K_{Tf},\ 10K_{Qf}\right)$ and pressure $\left(K_{Tp},\ 10K_{Qp}\right)$ components, computed for the propeller working at full scale.

Table A6. Radial distribution of the propeller coefficients computed for J = 0.1 at full scale.

$\Delta r/R = (r/R)_i – (r/R)_{i-1}$	r/R	K_{Tf}	K_{Tp}	K_T	$10K_{Qf}$	$10K_{Qp}$	$10K_Q$
d_h–0.30	0.2271	0.000200	0.010454	0.010653	0.000739	0.008230	0.008969
0.30–0.44	0.3700	0.000498	0.026079	0.026577	0.002218	0.024694	0.026912
0.44–0.57	0.5050	0.000857	0.044852	0.045709	0.004192	0.046670	0.050862
0.57–0.69	0.6300	0.001184	0.061939	0.063123	0.006088	0.067783	0.073871
0.69–0.80	0.7450	0.001349	0.070571	0.071920	0.006334	0.070519	0.076853
0.80–0.90	0.8500	0.001414	0.074008	0.075422	0.006267	0.069774	0.076041
0.90–0.975	0.9375	0.001057	0.055321	0.056378	0.004869	0.054211	0.059081
0.975–1.00	0.9875	0.000177	0.009257	0.009434	0.001232	0.013712	0.014943
Σ		0.006737	0.352480	0.359217	0.031940	0.355592	0.387532

Table A7. Radial distribution of the propeller coefficients computed for J = 0.3 at full scale.

$\Delta r/R = (r/R)_i – (r/R)_{i-1}$	r/R	K_{Tf}	K_{Tp}	K_T	$10K_{Qf}$	$10K_{Qp}$	$10K_Q$
d_h–0.30	0.2271	0.000201	0.008063	0.008264	0.00069	0.007175	0.007862
0.30–0.44	0.3700	0.000501	0.020116	0.020617	0.00206	0.021530	0.023591
0.44–0.57	0.5050	0.000862	0.034596	0.035458	0.00389	0.040691	0.044586
0.57–0.69	0.6300	0.001190	0.047776	0.048966	0.00566	0.059099	0.064756
0.69–0.80	0.7450	0.001356	0.054434	0.055790	0.00589	0.061485	0.067370
0.80–0.90	0.8500	0.001422	0.057085	0.058507	0.00582	0.060835	0.066658
0.90–0.975	0.9375	0.001063	0.042672	0.043734	0.00452	0.047266	0.051790
0.975–1.00	0.9875	0.000178	0.007140	0.007318	0.00114	0.011955	0.013099
Σ		0.006824	0.274003	0.271883	0.029935	0.312747	0.342681

Table A8. Radial distribution of the propeller coefficients computed for J = 0.5 at full scale.

$\Delta r/R = (r/R)_i – (r/R)_{i-1}$	r/R	K_{Tf}	K_{Tp}	K_T	$10K_{Qf}$	$10K_{Qp}$	$10K_Q$
d_h–0.30	0.2271	0.000216	0.005996	0.006212	0.000843	0.005524	0.006367
0.30–0.44	0.3700	0.000539	0.014958	0.015497	0.002530	0.016574	0.019104
0.44–0.57	0.5050	0.000927	0.025726	0.026653	0.004781	0.031324	0.036105
0.57–0.69	0.6300	0.001280	0.035527	0.036807	0.006944	0.045495	0.052439
0.69–0.80	0.7450	0.001458	0.040478	0.041936	0.007224	0.047332	0.054555
0.80–0.90	0.8500	0.001529	0.042450	0.043979	0.007147	0.046832	0.053979
0.90–0.975	0.9375	0.001143	0.031731	0.032874	0.005553	0.036386	0.041939
0.975–1.00	0.9875	0.000191	0.005310	0.005501	0.001405	0.009203	0.010608
Σ		0.007282	0.202178	0.209459	0.026426	0.238670	0.275096

Table A9. Radial distribution of the propeller coefficients computed for J = 0.7 at full scale.

$\Delta r/R = (r/R)_i – (r/R)_{i-1}$	r/R	K_{Tf}	K_{Tp}	K_T	$10K_{Qf}$	$10K_{Qp}$	$10K_Q$
d_h–0.30	0.2271	0.000255	0.003154	0.003409	0.000592	0.003468	0.004059
0.30–0.44	0.3700	0.000637	0.007869	0.008506	0.001776	0.010405	0.012181
0.44–0.57	0.5050	0.001096	0.013533	0.014629	0.003356	0.019665	0.023021
0.57–0.69	0.6300	0.001513	0.018689	0.020202	0.004874	0.028561	0.033435
0.69–0.80	0.7450	0.001724	0.021293	0.023017	0.005070	0.029714	0.034785
0.80–0.90	0.8500	0.001808	0.022330	0.024138	0.005017	0.029400	0.034417
0.90–0.975	0.9375	0.001351	0.016692	0.018043	0.003898	0.022843	0.026741
0.975–1.00	0.9875	0.000226	0.002793	0.003019	0.000986	0.005778	0.006764
Σ		0.008611	0.106352	0.114963	0.025568	0.149835	0.175402

Table A10. Radial distribution of the propeller coefficients computed for J = 0.9 at full scale.

$\Delta r/R = (r/R)_i – (r/R)_{i-1}$	r/R	K_{Tf}	K_{Tp}	K_T	$10K_{Qf}$	$10K_{Qp}$	$10K_Q$
d_h–0.30	0.2271	0.000107	0.000104	0.000211	0.000578	0.000643	0.001221
0.30–0.44	0.3700	0.000267	0.000259	0.000526	0.001735	0.001928	0.003663
0.44–0.57	0.5050	0.000460	0.000445	0.000904	0.003279	0.003644	0.006922
0.57–0.69	0.6300	0.000635	0.000614	0.001249	0.004762	0.005292	0.010054
0.69–0.80	0.7450	0.000723	0.000700	0.001423	0.004954	0.005506	0.010460
0.80–0.90	0.8500	0.000759	0.000734	0.001492	0.004902	0.005448	0.010349
0.90–0.975	0.9375	0.000567	0.000548	0.001116	0.003808	0.004233	0.008041
0.975–1.00	0.9875	0.000095	0.000092	0.000187	0.000963	0.001071	0.002034
Σ		0.004113	0.003494	0.007707	0.019981	0.027764	0.047744

References

1. Stanier, M. The Application of RANS Code to Investigate Propeller Scale Effects. In Proceedings of the 22nd ONR Symposium, Washington, DC, USA, 9–18 August 1998; pp. 222–238.
2. Funeno, I. On Viscous Flow around Marine Propellers—Hub Vortex and Scale Effect. *J. Kansai Soc. Nav. Archit.* **2002**, *238*, 17–27.
3. ITTC. 1978 ITTC Performance Prediction Method: Procedure 7.5-02-03-01.4. In Proceedings of the International Towing Tank Conference, West Bethesda, MD, USA, 3–5 December 2017; pp. 1–15.
4. Pérez Sobrino, M.; Minguito Cardeña, E.; Garcia Gómez, A.; Masip Hidalgo, J.; Quereda Laviña, R.; Pangusion Cidales, L.; Pérez Gómez, G.; Gonzalez-Adalid, J. Scale Effects in Model Tests with CLT Propellers. In Proceedings of the 27th Motor Ship Marine Propulsion Conference, Bilbao, Spain, 27–28 January 2005.
5. Helma, S. A scaling procedure for modern propeller designs. *Ocean Eng.* **2016**, *120*, 165–174. [CrossRef]
6. Helma, S.; Streckwall, H.; Richter, J. The Effect of Propeller Scaling Methodology on the Performance Prediction. *J. Mar. Sci. Eng.* **2018**, *6*, 60. [CrossRef]
7. Hsin, C.-Y.; Chang, K.-K.; Chi, R.-C.; Chen, P.-F. Design and Analysis of the End Plate Effect Propellers. In Proceedings of the 28th Symposium on Naval Hydrodynamics, Pasadena, CA, USA, 12–17 September 2010.
8. Sánchez-Caja, A.; González-Adalid, J.; Pérez-Sobrino, M.; Saisto, I. Study of End-Plate Shape Variations for Tip Loaded Propellers Using a RANSE Solver. In Proceedings of the 29th Symposium on Naval Hydrodynamics, Gothenburg, Sweden, 26–31 August 2012; pp. 26–31.
9. Andersen, P.; Friesch, J.; Kappel, J.J.; Lundegaard, L.; Patience, G. Development of a Marine Propeller with Nonplanar Lifting Surfaces. *Mar. Technol.* **2005**, *42*, 144–158.
10. Adalid, J.G.; Gennaro, G. Latest Experiences with Contracted and Loaded Tip (CLT) Propellers. In *Sustainable Maritime Transportation and Exploitation of Sea Resources*, 1st ed.; Taylor & Francis Group: London, UK, 2011; Volume 1, pp. 47–53.
11. Koushan, K.; Krasilnikov, V.I. Experimental and Numerical Investigation of Open Thrusters in Oblique Flow Conditions. In Proceedings of the 27th ONR Symposium on Naval Hydrodynamics, Seoul, Korea, 5–10 October 2008.
12. Krasilnikov, V.; Sun, J.; Halse, K.H. CFD Investigation in Scale Effect on Propellers with Different Magnitude of Skew in Turbulent Flow. In Proceedings of the 1st International Symposium on Marine Propulsors (SMP'09), Trondheim, Norway, 22–24 June 2009.
13. Müller, S.B.; Abdel-Maksoud, M.; Hilbert, G. Scale Effects on Propellers for Large Container Vessels. In Proceedings of the 1st International Symposium on Marine Propulsors (SMP'09), Trondheim, Norway, 22–24 June 2009.
14. Kawamura, T.; Omori, T. Reynolds Number Effect on Propeller Performance in Open Water. *J. Jpn. Soc. Nav. Archit.* **2009**, *10*, 29–36.
15. Li, D.Q.; Berchiche, N.; Janson, C.-E. Influence of Turbulence Models on the Prediction of Full-Scale Propeller Open Water Characteristics with RANS Methods. In Proceedings of the 26th Symposium on Naval Hydrodynamics, Rome, Italy, 17–22 September 2006.
16. Bhattacharyya, A.; Krasilnikov, V.; Sverre, S. Scale effects on open water characteristics of a controllable pitch Propeller working within different Duct Designs. *Ocean Eng.* **2016**, *112*, 226–242. [CrossRef]
17. Dong, X.-Q.; Wei Li, W.; Yang, C.-J.; Noblesse, F. RANSE-Based Simulation and Analysis of Scale Effects on Open-Water Performance of the PPTC-II Benchmark Propeller. *J. Ocean Eng. Sci.* **2018**, *3*, 186–204. [CrossRef]
18. Grabert, R.; Lubke, L.; Klose, R.; Barkmann, U. *ITTC Propeller Benchmark Tip Rake Propeller P172*; SVA-Report 4487; Schiffbau-Versuchsanstalt Potsdam: Potsdam, Germany, 2017.
19. Menter, F.R. Zonal Two Equation Kappa-Omega Turbulence Models for Aerodynamic Flows. In Proceedings of the 24th AIAA Fluid Dynamics Conference, Orlando, FL, USA, 6–9 July 1993.
20. Langtry, R.; Menter, F. Correlation-Based Transition Modeling for Unstructured Parallelized Computational Fluid Dynamics Codes. *AIAA J.* **2009**, *47*, 2894–2906. [CrossRef]
21. Lungu, A. Numerical Simulation of the Resistance and Self-Propulsion Model Tests. In Proceedings of the ASME 2018 37th International Conference on Ocean, Offshore and Arctic Engineering, Madrid, Spain, 17–22 June 2018.
22. Bekhit, A.S.; Lungu, A. Simulation of the POW Performance of the JBC Propeller. *AIP Conf. Proc.* **2019**, *2116*, 450007.

23. Guilmineau, E.; Deng, G.B.; Leroyer, A.; Queutey, P.; Visonneau, M.; Wackers, J. Influence of the Turbulence Closures for the Wake Prediction of a Marine Propeller. In Proceedings of the 4th International Symposium on Marine Propellers (SMP'15), Austin, TX, USA, 31 May–4 June 2015.
24. Eça, L.; Hoekstra, M. A Procedure for the Estimation of the Numerical Uncertainty of CFD Calculations Based on Grid Refinement Studies. *J. Comput. Phys.* **2014**, *262*, 104–130. [CrossRef]